Large low-frequency vibration attenuation induced by arrays of piezoelectric patches shunted with amplifier–resonator feedback circuits

2016 Smart Mater. Struct. 25 015004

(http://iopscience.iop.org/0964-1726/25/1/015004)

IOP Publishing Smart Materials and Structures
Smart Mater. Struct. 25 (2016) 015004 (15pp) doi:10.1088/0964-1726/25/1/015004

Large low-frequency vibration attenuation induced by arrays of piezoelectric patches shunted with amplifier–resonator feedback circuits

Gang Wang[1,2] **and Shengbing Chen**[3]

[1] State Key Laboratory of Advanced Design and Manufacturing for Vehicle Body, Hunan University, 410082 Changsha, People's Republic of China
[2] College of Mechanical and Vehicle Engineering, Hunan University, 410082 Changsha, People's Republic of China
[3] China Aerodynamics Research and Development Center, Mianyang 621000, People's Republic of China

E-mail: zaehwang@hotmail.com

Received 29 June 2015, revised 7 October 2015
Accepted for publication 13 October 2015
Published 17 November 2015

Abstract

Periodic arrays of piezoelectric patches shunted by amplifier–resonator circuits are attached to a beam in order to gain large low-frequency attenuations in the propagation of flexural beam vibration. A numerical model based on the transfer matrix methodology and Bloch theory are built to predict the band gaps and attenuation factors as well as the transmission of vibration in the proposed smart metamaterials. Influences of circuital parameters on attenuation factors and the equivalent Young's modulus are studied. It is found that the central frequency of attenuations is lower than the resonant frequency because of the negative equivalent elastic modulus of piezoelectric patches at frequencies lower than the resonance. Finite element simulations and vibration experiments are conducted on a 10 mm-thick aluminium alloy beam with six pairs of piezoelectric patches glued on it. Based on theoretical calculations, three sets of circuital parameters are chosen to gain large vibration transmission attenuations around the lowest three modal peaks. Significant attenuation is found in the experimental results, which is predicted in theoretical calculations and finite element simulations. A superlattice metamaterial specimen with a combination of three different sets of circuital parameters is also studied in order to gain wide attenuation frequency ranges.

Keywords: periodic structure, band gap, piezoelectric shunting, active vibration control, smart metamaterials

(Some figures may appear in colour only in the online journal)

1. Introduction

Innovative design of structures based on multiple physical principles represents a new trend as well as great challenge for the industrial and academic communities. For example, intensive efforts are dedicated to the integration of lightweight structures made of composite material in aerospace products, which brings new risks of fatigue and damage as well as problems of noise and vibration. Therefore, much effort has been expended on integrating smart materials or structures in order to implement structural health monitoring or vibration control on lightweight structures.

This paper contributes to the study of smart metamaterials, a new class of integration of smart materials or structures, in order to improve mechanical and vibroacoustic behaviors. The basic concepts underpinning smart metamaterials relate to periodic structure theories. Research on the propagation of elastic waves in periodic structures is well-developed [1].

A lot of work has focused on investigating pass and stop band behavior of periodic structures, which shows great potential in vibration isolation applications. Recently, the propagation of elastic or acoustic waves in phononic crystals by analogy with photonic crystals for electromagnetic waves has received enormous attention. For both electromagnetic and acoustic waves, the ordinary band gap is obtained by periodically modulating electromagnetic or mechanical properties [2], which is called the Bragg's band gap. Based on Bragg's mechanism, spatial periodicity should be of the same order as the wavelength in the band gap. Thus a large structure is always required in order to gain a low-frequency band gap. A solution to this problem is found in the locally resonant band gap mechanism first proposed by Liu *et al* [3], where the resonance of locally resonant units is the dominant factor in the formation of band gaps [4, 5]. More recently, research on locally resonant phononic crystals has been extended to a new class of metamaterials [6, 7]. Acoustic metamaterials are generally regarded as materials or structures with designed inner structures that possess abnormal physical behavior such as a band gap, directional propagation, negative refraction, acoustic cloaking, etc.

Another concept underpinning smart metamaterials is the use of smart materials such as piezoelectric ceramics (PZTs). With advantages such as being lightweight, and having facile and good performance, piezoelectric shunting has been used as an attractive technique for vibration and noise control. An elegant formulation of passive shunting was first proposed by Hagood and Von Flotow [8], and is still commonly used. The study showed how a PZT patch shunts through a resistor–inductor circuit, i.e. a resonant shunting circuit (RSC), acting as a tunable vibration absorber at the tuned resonance frequency of the circuit. Therefore, the resonant units of the metamaterials can also be obtained using an RSC connected to PZTs embedded on the surface of a hosting structure. The main benefit of such an idea lies in the elimination of the mechanical oscillators, which is crucial in the design of lightweight structures. In addition, the parameters of the electrical oscillator can be easily adjusted, which leads to smart behavior of the resulting structures. Moreover, resistance in shunting circuits can generate damping that allows the dissipation of energy, thus vibrations outside the band gaps may also be attenuated. The original periodic shunting concept was numerically demonstrated on rods and fluid-loaded axisymmetric shells by Thorp *et al* [9, 10]. Airoldi *et al* proposed the idea of generating multiple locally resonant band gaps in a beam by using multi-resonant shunts [11], and designed tunable metamaterials with periodic arrays of resonant shunted piezos [12]. We also performed some theoretical and experimental investigations on phononic rods [13] and beams [14] with passive shunting circuits and some useful conclusions were drawn. These studies demonstrated how resonant piezoelectric shunts can be utilized to manipulate the equivalent mechanical properties of an elastic waveguide, and therefore suggested their application in the development of tunable band gaps. This strategy has since been extended to flat plate hosting periodic arrays of shunted piezoelectric patches [15–19]. These works, based on the passive resonant shunting technique, cannot produce large attenuations in broad bands, especially in lower frequency ranges where the lowest vibration modes are located.

As a revision of the passive resonant shunting method, a negative capacitive strategy originally proposed by Forward [20] has received much attention [21–24]. In this configuration, a piezoelectric patch is shunted by a parallel or serial connection of an active impedance converter (with negative capacitance) and a passive shunting circuit. Therefore, the internal capacitance of the PZT patches is mainly canceled out. Although the negative capacitance shunting strategy has been experimentally validated [25], this technique actually requires the circuit to be tuned very close to the stability limit in order to obtain the desired performance [26]. Thus, small alterations may either destabilize the system or deteriorate the vibration control performance.

In order to enhance the locally resonant band gaps caused by the passive RSC, we previously proposed another active strategy, i.e. the enhanced RSC, in order to intensify the resonant effect of the passive RSC [27]. In the work, one of a pair of PZT patches glued on the hosting beam was connected with a passive RSC, while the voltage on it was amplified and added on the other PZT patch of the couple. As the amplification occurs after circuit resonance, it is named the 'resonator–amplifier' (R-A) shunting technique in this paper. Larger attenuations within a wide frequency range induced by arrays of R-A shunted PZT patches were illustrated compared with those induced by passive RSCs. However, the limit of such a circuit is that the in-port resistor of the reverse amplifier needs to be considered as a parallel connection of the inductor–resistor (RL) resonant circuit, which will in turn affect the oscillation itself. Furthermore, attenuation of the R-A shunt circuit within low-frequency ranges was still unsatisfactory.

Recently, Yamada *et al* proposed a new enhancing strategy for resonant shunting in a study on vibration damping of a cantilever [28]. In their work, the vibration signal measured is firstly amplified and then added on the PZT patch through an RL circuit; that is, the circuital resonance is moved after the amplifier. Due to its reverse order compared with the R-A shunting technique, it is called the 'amplifier–resonator' (A-R) technique in this paper. However, because the generalized impedance converter (GIC, also called Antoniou's circuits [14, 29]) used in order to achieve a large easily-tuned inductor with low self-resistance should be grounded at one end, two DC power supplies with two different reference points of the potential were necessary in the implementation of the technique.

In this paper, a model of one-dimensional (1D) metamaterials composed of periodic arrays of A-R shunted PZT patches attached to a beam is firstly built based on the transfer matrix (TM) method and Bloch's theory. Thereafter, theoretical predictions on band structures, attenuation factors as well as the transmission of flexural vibration in the proposed smart metamaterials are made, and the vibration attenuation feature of the A-R and R-A shunting circuits compared. Secondly, variations of level and frequency range of the vibration attenuation with different circuital parameters are studied,

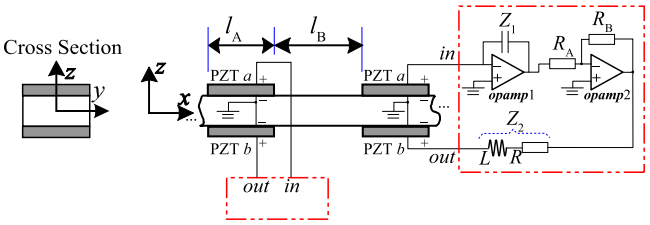

Figure 1. Periodic arrays of amplifier–resonator piezoelectric shunting on a beam.

where the physical mechanism of the band gap is discussed. Thirdly, the implementing techniques of both the A-R and R-A shunting circuits are discussed. Floating virtual inductors are applied in order to avoid the use of two DC power supplies in the A-R shunting, and the previously proposed R-A shunting circuit is also adapted in order to eliminate the above mentioned shortage. Finally, finite element method (FEM) simulations and vibration experiments are conducted on a 10 mm-thick aluminium alloy beam with six pairs of piezoelectric patches glued on it. Experimental results are compared with those of theoretical calculations and FEM simulations in order to validate the theoretical results.

2. Theoretical analysis

2.1. Modeling and calculation method

As illustrated in figure 1, pairs of PZT patches are periodically glued to the upper and lower surfaces of a beam. The constructed periodic structure can be considered a 1D metamaterial. Each pair of PZT patches is placed with opposite polarizing directions along the z-axis and connected with a shunting circuit. All shunting circuits are the same and separated so that they can work independently under the same mechanism. Thus the periodicity of the smart structure is guaranteed. The beam's segments with the PZT patch are denoted by A, while the others are denoted by B. Each shunting circuit is composed of a charge amplifier, voltage amplifier and RL circuit. Considering the inherent capacity of PZT patch b, the RL circuit becomes an LC resonator. In detail, the charge on PZT patch a caused by the deformation of the beam is transformed into a voltage which is amplified by two operational amplifiers (opamp). Then the amplified voltage signal is fed back to PZT patch b through the RL circuit. The acting order of the A-R shunting circuit in figure 1 is 'magnification before resonance', which is opposite to the enhanced resonant shunting method [27] (also called R-A shunting in this paper because the amplifier is placed after the resonator) proposed in our previous work.

Except surfaces along the xy-plane, all faces of PZT patches are supposed to be free of constraints. Therefore, the piezoelectric equations are [10]

$$\begin{bmatrix} S_1^a \\ D_3^a \end{bmatrix} = \begin{bmatrix} s_{11}^{\mathrm{E}} & d_{31} \\ d_{31} & \varepsilon_{33}^{\mathrm{T}} \end{bmatrix} \begin{bmatrix} T_1^a \\ E_3^a \end{bmatrix}, \quad (\text{PZT } a) \tag{1}$$

$$\begin{bmatrix} S_1^b \\ D_3^b \end{bmatrix} = \begin{bmatrix} s_{11}^{\mathrm{E}} & d_{31} \\ d_{31} & \varepsilon_{33}^{\mathrm{T}} \end{bmatrix} \begin{bmatrix} T_1^b \\ E_3^b \end{bmatrix}, \quad (\text{PZT } b) \tag{2}$$

where 1, 2 and 3 denote coordinates x, y and z, respectively; S_1^a, S_1^b, T_1^a, T_1^b are the mechanical strain and stress of upper (denoted by a) and lower (denoted by b) PZT patches along the x-axis; E_3^a, E_3^b, D_3^a, D_3^b are the electric field and electric displacement of the PZT patches a and b, respectively; s_{11}^{E} is the compliance coefficient of the PZT material at constant electric field intensity; d_{31} is the piezoelectric strain constant; and $\varepsilon_{33}^{\mathrm{T}}$ is the dielectric constant of the PZT material.

When a harmonic vibration is assumed, the electric current I_a generated by the PZT patch a can be written as

$$I_a = -A_s D_3^a s, \tag{3}$$

where $s = \mathrm{i}\omega$ is the Laplace operator, ω is the angular frequency and A_s is the area of the PZT electrode.

Under ideal conditions, the voltages of the positive and negative inputting ports of an opamp are approximately the same, and the inward or outward current is nearly 0. So the PZT patch a is equivalently grounded, and the voltage V_1 on the output node of opamp1 is

$$V_1 = -I_a Z_1 = A_s D_3^a Z_1 s, \tag{4}$$

where a capacitor C is commonly used as Z_1, thus $Z_1 = 1/Cs$.

The voltage V_2 on the output node of opamp2 is a negative amplification of V_1, thus

$$V_2 = -\frac{R_B}{R_A} V_1 = -\alpha V_1, \tag{5}$$

where $\alpha = R_B/R_A$ is the amplifying ratio.

The current I_b flow in the PZT patch b is

$$I_b = A_s D_3^b s = \frac{V_2 - E_3^b h_p}{Z_2}, \tag{6}$$

where h_p is the thickness of all PZT patches, and $Z_2 = R + Ls$ is the sum of impedances of R and L in serial connection.

As PZT patch a is equivalently grounded $(E_3^a = 0)$, equation (1) can be reduced to

$$\begin{cases} S_1^a = s_{11}^{\mathrm{E}} T_1^a \\ D_3^a = d_{31} T_1^a. \end{cases} \tag{7}$$

The equivalent elastic modulus of PZT patch a, E_p^a can be written as mechanical stress divided by strain,

$$E_p^a = \frac{T_1^a}{S_1^a} = \frac{1}{s_{11}^{\mathrm{E}}}. \tag{8}$$

Substituting equation (7) into (4), we have

$$V_1 = A_s d_{31} Z_1 \frac{S_1^a}{s_{11}^{\mathrm{E}}} s. \tag{9}$$

As for the bending deformation of the composite beam, the mechanical strains of PZT patches a and b in one pair are nearly inverse values,

$$S_1^a = -S_1^b. \tag{10}$$

Substituting equation (9) into equation (5), and then in equation (6) along with equation (10), we get

$$A_s D_3^b s = \left(\alpha A_s d_{31} Z_1 \frac{S_1^b}{s_{11}^{\mathrm{E}}} s - E_3^b h_p \right) / Z_2. \tag{11}$$

Combining equations (2) and (11), we can obtain the equivalent elastic modulus E_p^b of PZT patch b as

$$E_p^b = \frac{T_1^b}{S_1^b} = \frac{-\alpha A_s Z_1 (d_{31})^2 s + s_{11}^{\mathrm{E}} h_p + A_s s_{11}^{\mathrm{E}} Z_2 \epsilon_{33}^{\mathrm{T}} s}{s_{11}^{\mathrm{E}} \left[-A_s Z_2 (d_{31})^2 s + s_{11}^{\mathrm{E}} h_p + A_s s_{11}^{\mathrm{E}} Z_2 \epsilon_{33}^{\mathrm{T}} s \right]}. \tag{12}$$

If each segment A or B of the beam can be considered under the Euler–Bernoulli condition, the flexural elastic waves in it are governed by the differential equations

$$EI \frac{\partial^4 u(x,t)}{\partial x^4} + \rho A \frac{\partial^2 u(x,t)}{\partial t^2} = 0, \tag{13}$$

where $u(x, t)$ is the displacement of the beam along the z-axis. EI, ρ and A are, respectively, the bending rigidity, density and cross-section area, which are different for every segment. For example, EI and ρA in segment B can be described by

$$EI|_{\mathrm{B}} = E_{\mathrm{beam}} \frac{b_1 h_1^3}{12}, \quad \rho A|_{\mathrm{B}} = \rho_{\mathrm{beam}} b_1 h_1, \tag{14}$$

where E_{beam} and ρ_{beam} are the elastic modulus and density of the hosting beam, while b_1 and h_1 are the width and thickness of the beam.

Similarly, EI and ρA in beam segments A can be calculated as the sum of bending rigidities and linear density of the beam and the PZT patches,

$$EI|_{\mathrm{A}} = E_{\mathrm{beam}} \frac{b_1 h_1^3}{12} + \left(E_p^a + E_p^b \right) \left[\left(\frac{h_1}{2} \right)^2 + \frac{h_1 h_p}{2} + \frac{h_p^2}{3} \right] \times b_p h_p, \quad \rho A|_{\mathrm{A}} = \rho_{\mathrm{beam}} b_1 h_1 + 2 \rho_p b_p h_p, \tag{15}$$

where ρ_{p} and b_p are the density and width of the PZT patch.

If harmonic vibrations in beam segments A or B are assumed as $u_{\mathrm{A,B}}(x, t) = u_{\mathrm{A,B}}(x) \mathrm{e}^{\mathrm{i}\omega t}$, the solution of wave equation (13) is in the form of

$$u_{\mathrm{A,B}}(x) = \left[\cos(\lambda_{\mathrm{A,B}} x) \quad \sin(\lambda_{\mathrm{A,B}} x) \quad \cosh(\lambda_{\mathrm{A,B}} x) \quad \sinh(\lambda_{\mathrm{A,B}} x) \right] \psi_{\mathrm{A,B}}, \tag{16}$$

where $\lambda_{\mathrm{A,B}} = \sqrt[4]{\omega^2 (\rho \mathrm{A}|_{\mathrm{A,B}}) / (EI|_{\mathrm{A,B}})}$ is the wave number in beam A or B, and $\psi_{A,B} = \{A, B, C, D\}^{\mathrm{T}}$ are factors that need to be determined.

In period n, the continuity of displacement, rotating angle, bending moment and shearing force at the boundary of beam segments A and B ensures that

$$\mathbf{H}_{\mathrm{A}}(l_{\mathrm{A}}) \psi_{\mathrm{A},n} = \mathbf{H}_{\mathrm{B}}(0) \psi_{\mathrm{B},n}. \tag{17}$$

The continuity at the boundary of beam segment B in period n and beam segment A in period $n + 1$ ensures

$$\mathbf{H}_{\mathrm{B}}(l_{\mathrm{B}}) \psi_{\mathrm{B},n} = \mathbf{H}_{\mathrm{A}}(0) \psi_{\mathrm{A},n+1}, \tag{18}$$

where

$$\mathbf{H}_{\mathrm{A,B}}(l) = \begin{bmatrix} \cos(\lambda_{\mathrm{A,B}} l) \\ -\lambda_{\mathrm{A,B}} \sin(\lambda_{\mathrm{A,B}} l) \\ -EI|_{\mathrm{A,B}} (\lambda_{\mathrm{A,B}})^2 \cos(\lambda_{\mathrm{A,B}} l) \\ EI|_{\mathrm{A,B}} (\lambda_{\mathrm{A,B}})^3 \sin(\lambda_{\mathrm{A,B}} l) \\ \sin(\lambda_{\mathrm{A,B}} l) \\ \lambda_{\mathrm{A,B}} \cos(\lambda_{\mathrm{A,B}} l) \\ -EI|_{\mathrm{A,B}} (\lambda_{\mathrm{A,B}})^2 \sin(\lambda_{\mathrm{A,B}} l) \\ -EI|_{\mathrm{A,B}} (\lambda_{\mathrm{A,B}})^3 \cos(\lambda_{\mathrm{A,B}} l) \\ \cosh(\lambda_{\mathrm{A,B}} l) \\ \lambda_{\mathrm{A,B}} \sinh(\lambda_{\mathrm{A,B}} l) \\ EI|_{\mathrm{A,B}} (\lambda_{\mathrm{A,B}})^2 \cosh(\lambda_{\mathrm{A,B}} l) \\ EI|_{\mathrm{A,B}} (\lambda_{\mathrm{A,B}})^3 \sinh(\lambda_{\mathrm{A,B}} l) \\ \sinh(\lambda_{\mathrm{A,B}} l) \\ \lambda_{\mathrm{A,B}} \cosh(\lambda_{\mathrm{A,B}} l) \\ EI|_{\mathrm{A,B}} (\lambda_{\mathrm{A,B}})^2 \sinh(\lambda_{\mathrm{A,B}} l) \\ EI|_{\mathrm{A,B}} (\lambda_{\mathrm{A,B}})^3 \cosh(\lambda_{\mathrm{A,B}} l) \end{bmatrix}. \tag{19}$$

Combining equations (17) and (18), we can get

$$\psi_{\mathrm{A},n+1} = \mathbf{T} \psi_{\mathrm{A},n}, \tag{20}$$

where $\mathbf{T} = [\mathbf{H}_{\mathrm{A}}(0)]^{-1} \mathbf{H}_{\mathrm{B}}(l_{\mathrm{B}}) [\mathbf{H}_{\mathrm{B}}(0)]^{-1} \mathbf{H}_{\mathrm{A}}(l_{\mathrm{A}})$ is the transfer matrix between adjacent periods of the beam.

For the infinite period structure illustrated in figure 1, the Bloch boundary condition [30] on the beam can be described as

$$\psi_{\mathrm{A},n+1} = \mathrm{e}^{\mathrm{i}qa} \psi_{\mathrm{A},n}, \tag{21}$$

where qa is the wave propagation constant in the infinite periodic structure, which consists of the wave vector (real part) and the attenuation factor μ (imaginary part); $a = l_{\mathrm{A}} + l_{\mathrm{B}}$ is the lattice constant of the 1D metamaterial; and l_{A} and l_{B} are the lengths of beam segments A and B.

Combining equation (21) with (20), an eigenvalue equation can be derived,

$$\left| \mathbf{T} - \mathrm{e}^{\mathrm{i}qa} \mathbf{I} \right| = 0. \tag{22}$$

For a given ω, we can calculate the corresponding propagation constant qa with equation (22). The real part of q is the wave number, which is used to describe wave phenomena. When q is a real number, a flexural wave can propagate freely in the infinite metamaterial structure. The graph of wave number versus frequency is called the band structure. In contrast, a complex q means that the wave is in a band gap. The attenuation constant $\mu = \mathrm{imag}(qa)$ indicates the

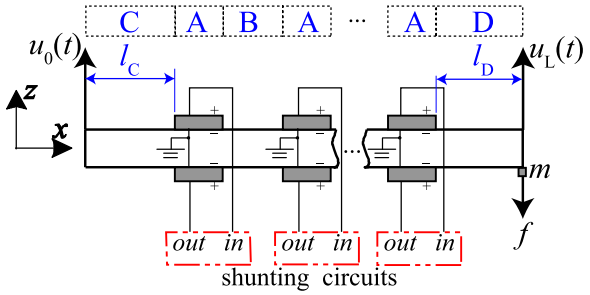

Figure 2. A specimen of the 1D piezoelectric metamaterial and its boundary conditions.

attenuation of the amplitude when the elastic wave propagates from one period to the next.

For a specimen of 1D metamaterial with finite dimension, the vibration transmission frequency response function (FRF) specifies the ratio of vibration transmitted from one point of the beam to another. An N-period finite sample with free restriction, a given displacement $u_0(t)$ as excitation and an added mass m for vibration measurements is illustrated in figure 2, where segments C and D with lengths l_C and l_D are the edging segments near the excitation and sensor, respectively. Thus the total length of the specimen is $l_{total} = (N-1)a + l_A + l_C + l_D$.

Based on the TM method, the factor vectors ψ_C and ψ_D of the wave equation in beam segments C and D have the relationship

$$\psi_D = \mathbf{T}_{all}\psi_C, \tag{23}$$

where $\mathbf{T}_{all} = [\mathbf{H}_D(0)]^{-1}\mathbf{H}_A(l_A)\mathbf{T}^{N-1}[\mathbf{H}_A(0)]^{-1}\mathbf{H}_C(l_C)$ is the total transfer matrix, and N is the total number of periods in this finite sample.

When normalized displacement excitation $u_0(t) = e^{i\omega t}$ is assumed, the boundary conditions on the left and right sides of the beam are

$$\begin{aligned}\mathbf{H}_C(0)\psi_C &= \begin{bmatrix}1 & \theta_0 & 0 & Q_0\end{bmatrix}^T \\ \mathbf{H}_D(l_D)\psi_D &= \begin{bmatrix}u_L & \theta_0 & 0 & \omega^2 m\mathbf{H}_D(l_D)_{1,:}\psi_D\end{bmatrix}^T\end{aligned} \tag{24}$$

where $\mathbf{H}_D(l_D)_{1,:}$ represents the first row and column of $\mathbf{H}_D(l_D)$, and m is the mass of possible sensor attached on the right end of the beam used for vibration measurements.

Combining equations (24) and (23) in matrix form leads to

$$\begin{bmatrix}\mathbf{H}_C(0)_{1,:} & \mathbf{0} \\ \mathbf{H}_C(0)_{3,:} & \mathbf{0} \\ \mathbf{0} & \mathbf{H}_D(l_D)_{3,:} \\ \mathbf{0} & \mathbf{H}_D(l_D)_{4,:} - \omega^2 m\mathbf{H}_D(l_D)_{1,:} \\ \mathbf{T}_{all} & -\mathbf{I}\end{bmatrix}\begin{pmatrix}\psi_C \\ \psi_D\end{pmatrix} = \begin{pmatrix}1 \\ 0 \\ 0 \\ 0 \\ \mathbf{0}\end{pmatrix}. \tag{25}$$

By solving equation (25), we can get the factor vectors ψ_C and ψ_D, and thus the transmission FRF between $u_0(t)$ and $u_L(t)$ can be calculated as

$$\mathrm{FRF} = 20\log_{10}\left[\mathbf{H}_D(l_D)_{1,:}\psi_D\right]. \tag{26}$$

Table 1. Geometric and material parameters of the hosting beam (aluminum alloy 6061-T6).

Parameter	Symbol	Value
Density	ρ_{beam}	2700 kg m^{-3}
Young's modulus	E_{beam}	69.5 GPa
Width	b_1	0.04 m
Thickness	h_1	0.01 m
Length of segment A	l_A	0.04 m
Length of segment B	l_B	0.06 m
Mass of sensor	m	8 g
Number of periods	N	6
Length of segment C	l_C	0.13 m
Length of segment D	l_D	0.13 m

Table 2. Geometric and material parameters of the piezoelectric patch (P-42).

Parameter	Symbol	Value
Density	ρ_{beam}	7600 kg m^{-3}
Compliance coefficient	S_{11}^E	11×10^{-12} m^2 N^{-1}
Piezoelectric strain constant	d_{31}	-101×10^{-12} C N^{-1}
Dielectric constant	ε_{33}^T	1.2390×10^{-8} F m^{-1}
Width	b_p	0.04 m
Thickness	h_p	1×10^{-3} m

Table 3. Circuital parameters.

Parameter	Symbol Value	Set-0	Value Set-1	Value Set-2	Value Set-3
Amplifier	α	9.5	9.5	17.6	17.6
Inductor	L	302 H	302 H	25 H	6 H
Resistor	R	0 Ω	5 kΩ	5 kΩ	5 kΩ
Capacitor	C			15 nF	

In order to exhibit the large low-frequency attenuation induced by periodic arrays of A-R piezoelectric shunting on a beam, we constructed a 1D metamaterial which consisted of a 10 mm-thick aluminum alloy (6061-T6) beam and six pairs of piezoelectric patches (material type P-42) glued on it. The geometric and material parameters employed in the calculations are listed in tables 1 and 2. The lattice constant (i.e. the length of one period) is $a = l_A + l_B = 0.1$ m, and the total length of the finite sample is thus $l_{total} = (N-1)a + l_A + l_C + l_D = 0.8$ m. Four sets of circuital parameters of the A-R shunting circuit listed in table 3 are selected in the calculations.

The above-mentioned calculation methods are based on the assumption that the strain and electric displacement are uniform, thus the effect of the shunted PZT patch can be regarded as equivalent to the elastic modulus. This

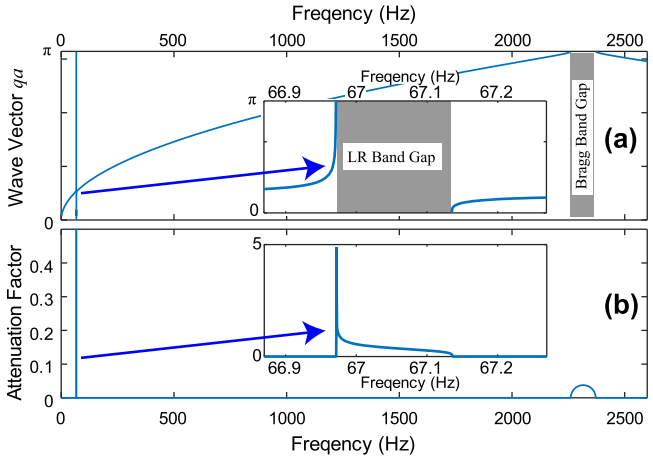

Figure 3. Calculated (a) band structure and (b) attenuation constants of the 1D piezoelectric metamaterials. The inner subfigures are zoom-in views of the locally resonant band gap. Parameter set-0 is used in the calculation.

assumption is correct in the lower frequency range when the whole area of one PZT patch is approximately in equal tension or compression states synchronously. As for higher frequency ranges, this assumption may be inaccurate and lead to errors. When the assumption of uniform strain is discarded, one can deduce that the shunting effect should be treated as an appended stress on the PZT patches [13]. We found that the method in this paper is precise enough in frequency ranges lower than half the Bragg band gap. In this paper, we are concerned mostly with the control of vibration in lower frequency ranges, which is far lower (e.g. see figure 3) than the Bragg band gap frequencies.

2.2. Band structures

The propagation constant q cannot be a pure real number when damping effects are involved, so that band structures do not exist when resistors are involved. In order to demonstrate the band structure of the proposed period structure, resistor R is set to 0 in order to eliminate damping in circuits.

Figures 3(a) and (b) illustrate the calculated band structure and attenuation constants of the 1D metamaterials with A-R piezoelectric shunting, where circuital parameter set-0 in table 3 is used in the calculation. The shaded areas denote band gaps where the propagation of flexural waves is forbidden in ideal infinite periodic structures. The first Bragg band gap is between 2260 Hz and 2371 Hz, while an extremely narrow band gap can also be found between 66.97 Hz and 67.13 Hz which is far lower than the frequency range of the Bragg one. The phase shift of the dispersion curve in figure 3(a) from π to 0 is found at the edges of the ultralow frequency gap, which indicates that it is based on the locally resonant band gap mechanism.

In the band gap, energy is localized or reflected to its source because no absorption exists. Due to the absence of damping, the attenuation factor is always zero at frequencies out of band gaps. Thus the flexural wave can propagate freely with a specified wave vector $q(\omega)$.

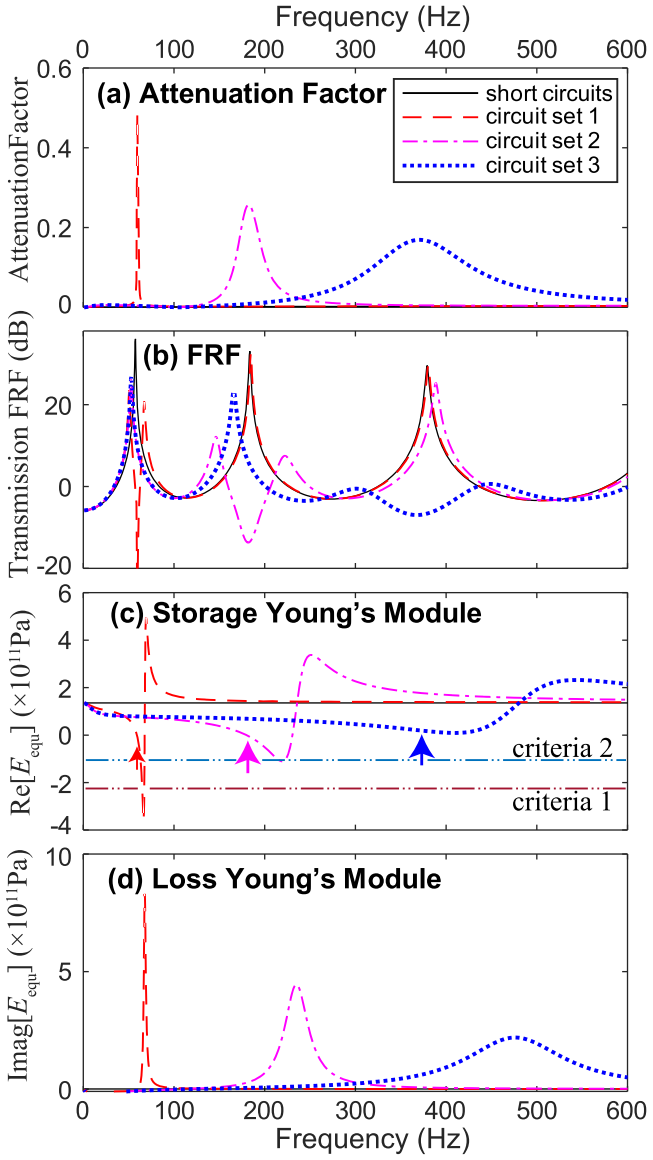

Figure 4. Calculated (a) attenuation factor and (b) vibration transmission FRF of the 1D piezoelectric metamaterials with A-R shunting circuits, as well as the equivalent (c) storage and (d) loss Young's moduli of beam segment A (with PZT patches). The solid line represents the results when all the PZT patches are shorted, while the dashed, dash-dotted and dotted lines correspond to that when A-R shunting circuits with parameter sets 1–3 are used, respectively. The two-dot-chain lines in subfigure (c) denote the positions of criteria 1 and 2 discussed in section 2.6.

2.3. Attenuation factor and transmission FRF

Although the peak of the attenuation factor in the locally resonant band gap is nearly 5, as illustrated in figure 3, the gap of such a metamaterial without damping is too narrow to be used in real situations. Damping added in the circuit is an effective way to widen it. However, for periodic structures with damping, the real part of the propagation constant qa is always non-zero even in the band gaps. So the attenuation factor becomes the last effective way to describe the band gap phenomenon in infinite periodic structures. At the same time, for the finite sample of the infinite structure, vibration

transmission FRF is still an effective way to specify the actual effect of the band gap mechanism.

Figures 4(a) and (b) illustrate the calculated attenuation factor and vibration transmission FRF of the 1D smart metamaterials, respectively. In the calculation of the FRF, a finite sample with six periods, hosting beam segments C and D as well as the adding mass m of a sensor is considered. These additional parameters are listed in table 1. Circuital parameter sets 1–3 (see table 3) are used in the calculations, while the corresponding results are plotted as dashed, dash-dotted and dotted lines, respectively. In order to study the mechanism of the locally resonant band gap, the real and imaginary parts of the equivalent Young's modulus E_{equ} of beam segment A calculated with equation (27) are illustrated in figures 4(c) and (d). The real and imaginary parts of it are also called the storage and loss Young's modulus. They can be used as a reference to determine the resonant frequency of a damped oscillator connected to a structure. Specifically, the oscillator's resonant frequency is ordinarily where the equivalent loss Young's modulus reaches a maximum while the storage one is the reverse,

$$E_{\text{equ}}(\omega) = \frac{EI|_{\text{A}}(\omega)}{I_{\text{beam}}} = \frac{12EI|_{\text{A}}(\omega)}{\left(b_1 h_1^3\right)}. \tag{27}$$

Furthermore, the solid lines in figure 4 represent the calculated results for the same structure while all PZT patches are shorted for comparison. From the solid line in figure 4(b), three modal peaks below 500 Hz can be observed, which is due to the 'standing wave' effect caused by boundary conditions of the finite structure. Within the modal peak, the vibration can easily propagate from the excitation side of the hosting beam to the other, and often with an amplitude much larger than its original source. Circuital parameter sets 1–3 are chosen in order to tune the attenuation frequency to match the frequencies of modes 1–3, respectively.

In figure 4, large attenuation factors can be found in the band gaps around 59 Hz, 182 Hz and 370 Hz. However, the highly sharp attenuation peak illustrated in figure 3(b) is averaged to a much wider frequency range (see figure 4(a)) while the maximum attenuation constant is decreased from nearly 5 to 0.5 by the damping effects of resistances. As the inductance L in the A-R circuit decreases, the attenuation peak caused by the locally resonant band gap moves to higher frequency ranges. Within the band gaps, the original modal peaks in the transmission FRF curve (corresponding to the case when all PZT patches are shorted) are greatly weakened. Compared with the curves of storage and loss Young's moduli, one can see that each attenuation peak corresponds to a frequency a little lower than the resonant frequency of the A-R shunting circuit, as noted by small arrows in figure 4(c). In these regions, the effective modulus of the PZT patches is negative, thus leading to a decrease of the equivalent Young's modulus of beam segment A. So, at these frequencies, the whole system can be considered as a periodic beam with segments A of very soft (even negative) elastic modulus, and thus the low-frequency band gap occurs based on the Bragg mechanism.

2.4. Comparison with the passive RSC and the R-A shunting techniques

In figure 5, the attenuation effect induced by the A-R shunting technique (dash-dotted lines) is compared with that caused by R-A shunting (dashed lines) and the passive RSC (dotted lines). The solid lines still represent the results when all PZT patches are shorted. For fair comparison, the amplifying ratio α and resistor R in different kinds of shunting circuits are fixed as in table 3 (sets 1–3), while the inductors in passive RSC and R-A shunt circuits are set to different values (as noted in figure 5) in order to adjust the maximum attenuation to the same frequency. At the same time, the in-port resistor (see R_{A} in figure 11(a) for reference) of the opamp in the R-A shunting circuit is set to infinity in order to eliminate its parallel connection effect and gain better performance. The implementation of this setting will be discussed in section 3.2.

It is obviously that the attenuation caused by the A-R shunting circuits is larger and wider compared with that induced by the R-A shunting circuits, while the R-A shunting technique is better than the passive RSC. For example, at the original second modal frequency, the attenuation of the A-R shunting is 11.49 dB larger than the R-A one, while the difference between the R-A and the passive RSC is 14.85 dB. Correspondingly, the drop of the equivalent modulus caused by the A-R circuits is also much larger than that by the R-A ones, and larger than that induced by passive ones. Another interesting feature in figure 5 is that the resonant frequency is higher than the attenuation frequency. It means that for the A-R shunting technique one can choose a smaller inductor L in order to gain the maximum attenuation at the same frequency. This feature is positive for low-frequency vibration control.

2.5. Parametric influences on attenuation factor

Figure 6 illustrates the influences of inductor L on the attenuation factors as well as the storage/loss Young's moduli of beam segment A (with PZT patches) of the 1D A-R shunted smart metamaterials. Other circuital parameters are fixed as in the table inside figure 6.

Both the frequency and the inductance in figure 6 are on a logarithmic scale, so that the relation between them appears linear. The fitting function between the central frequency f of attenuation and the inductor L can be written as follows, which is also plotted as the dash-dotted line in figure 6(c),

$$\begin{aligned} &\log_{10}(f) = k_1 \log_{10}(L) + k_2, \\ &\left(k_1 = -0.4985,\ k_2 = 3.0214\right). \end{aligned} \tag{28}$$

Figure 7 shows how the attenuation factor and equivalent storage/loss Young's moduli of beam segment A (with PZT patches) of the 1D A-R shunted smart metamaterials vary with the amplifying ratio α and the resistor R. As the variety

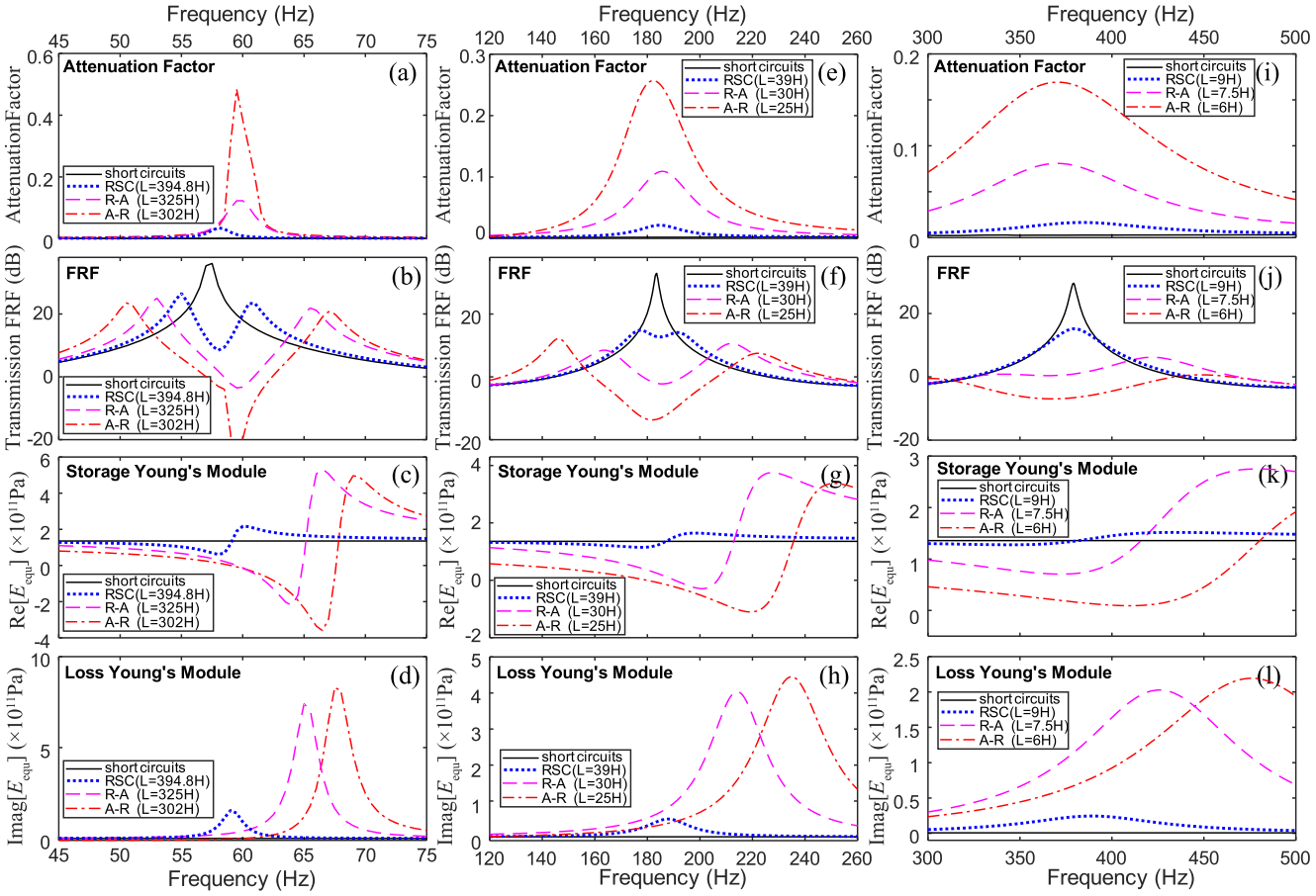

Figure 5. Comparison of the calculated (a), (e), (i) attenuation factor, (b), (f), (j) vibration transmission FRF, equivalent (c), (g), (k) storage and (d), (h), (l) loss Young's moduli of beam segment A (with PZT patches) of the 1D metamaterial with different kinds of resonant shunting circuits. The solid line represents the results when all the PZT patches are shorted, and the dash-dotted, dashed and dotted lines correspond to the results induced by A-R, R-A and passive RSC, respectively.

law with different inductors is similar, $L = 25$ H is chosen for representation. In figures 7(a)–(c), it can be seen that when the amplifying ratio increases, the frequency region of the negative equivalent storage modulus expands in the low-frequency direction, while the resonant frequency (i.e. the zero-crossing of the storage modulus as well as the peak of the loss modulus) remains unchanged. As discussed before, the decreasing of the equivalent Young's modulus of beam segment A is the main cause of the band gap, so the resulting attenuation peak shifts to lower frequencies when the amplifying ratio increases. In figures 7(d)–(f), we can also see that the frequency of the attenuation peak is not related to resistance R. However, when the resistance R increases, the maximum attenuation factor decreases, while the attenuation frequency region expands.

2.6. Stability

The stability of the proposed active shunting techniques is guaranteed by keeping the effective elastic modulus of the composite beam positive. A negative modulus will cause unphysical phenomena which may be unstable.

The effective Young's modulus of composite beam segments A calculated by equation (27) is a complex number. The imaginary part is the loss modulus which consumes energy, while the real part is the storage modulus that can store or release potential energy. Before carrying out the experiment, we need to ensure that the total effective storage modulus of the test sample keeps positive within the analyzing frequency ranges. Two criteria are established in this paper to guarantee the stability of the system.

The first criterion aims at the lowest vibration mode, where the whole composite beam vibrates like a static bending of a simple beam. The total equivalent Young's modulus must be positive, thus it can be approximatively described as

$$E_{\text{equ}} > -E_{\text{beam}} \frac{l_{\text{total}} - Nl_{\text{A}}}{Nl_{\text{A}}} \tag{29}$$

where l_{total} is the total length of the finite sample beam.

For the case when periodic number $N = 6$, equation (29) can be simplified to $E_{\text{equ}} < -3.17E_{\text{beam}}$.

The second criterion is designed to suit the higher vibration modes. In this case, it will be safer if we keep the equivalent Young's modulus in one period of the beam

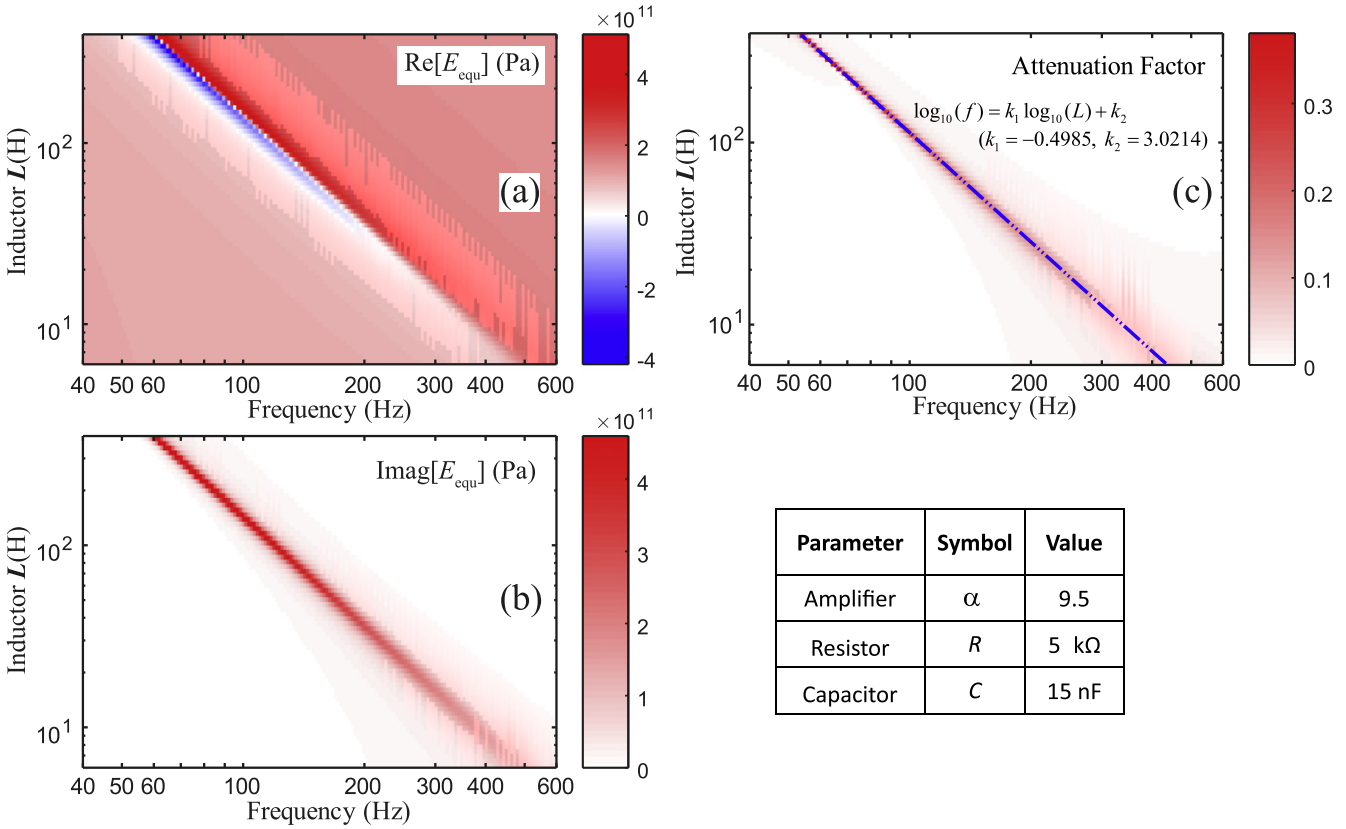

Parameter	Symbol	Value
Amplifier	α	9.5
Resistor	R	5 kΩ
Capacitor	C	15 nF

Figure 6. Calculated equivalent (a) storage and (b) loss Young's moduli of beam segment A (with PZT patches), as well as the (c) attenuation factors of the 1D A-R shunted smart metamaterials for different inductors L. Different colors represent different value of elastic moduli or attenuation factors. Other circuital parameters are listed in the table inside.

positive, thus

$$E_{\text{equ}} > -E_{\text{beam}} \frac{l_{\text{B}}}{l_{\text{A}}} = -1.5 E_{\text{beam}}. \tag{30}$$

Criteria 1 and 2 are plotted as two-dot-chain lines in figure 4(c). When the amplifying ratio increases, the effective elastic modulus around the circuital resonant frequency decreases and even becomes negative. If the criteria line is cut across, the corresponding parameters may cause instability and should be carefully avoided.

However, criteria 1 and 2 are a little bit conservative because the large equivalent loss modulus at the resonant frequency is not considered. In the experiment, we actually tune the amplifying ratio value to be as large as acceptable so that the test sample will not fall into self-excited vibrations. Circuital parameter sets 1 and 2 are chosen in this way, which are slightly over criteria 1 and 2, respectively.

3. Implementation of the shunt circuits

3.1. A-R shunting circuit with single reference of ground

A shunting circuit with resonance in the lower frequency range requires the using of a large inductor (even as large as several hecto-Henrys) with low resistance which is implemented through synthetic inductors [31]. The most common example of a synthetic inductor is Antoniou's circuit, as depicted in figure 8(a). The resulting inductance can be calculated with

$$L = \frac{R_1 R_3 R_5}{R_2} C_4. \tag{31}$$

The limit of Antoniou's circuit is that one terminal of the synthetic inductor has to be grounded. However, both terminals the inductor L in figure 1 cannot be grounded. Yamada's used two dc power supplies with two different reference points of the potential in order to solve the problem [28].

In order to trim the additional dc power, our first solution is to exchange the order of the PZT patch b and the inductor in the shunting circuit, as illustrated in figure 9. As one end of the inductor is grounded, Antoniou's circuit can still be used as the synthetic inductor, while the whole circuit has only one reference of ground. However, both terminals of the PZT patch b are of floating potentials in this case. This will cause system malfunction if PZT patches are glued on a conducting medium such as metal.

The other solution is the use of a floating synthetic inductor in the original circuit shown in figure 1. The sketch of the new synthetic inductor is depicted in figure 8(b). Two Antoniou's circuits in series interfering with each other share a common floating ground inside, thus the grounding of the outer terminal

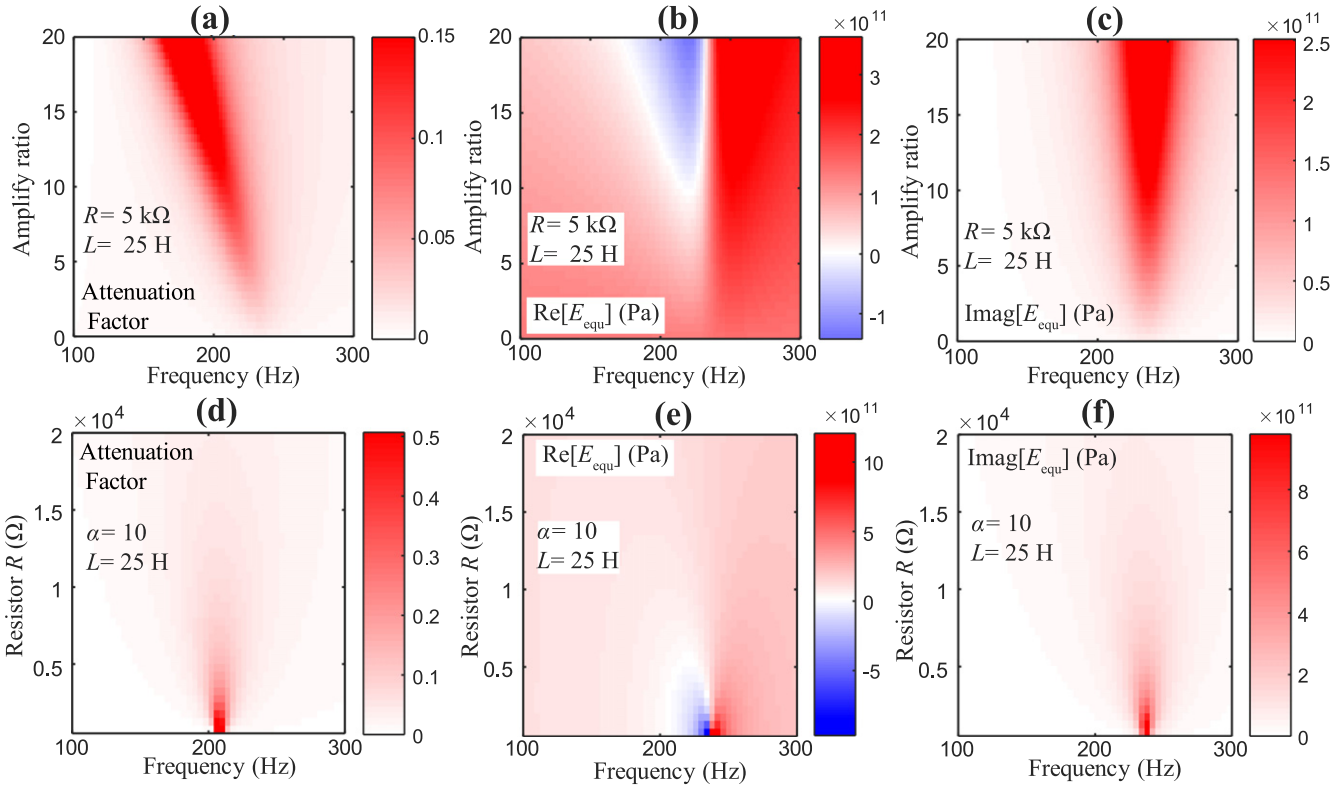

Figure 7. Variations of (a), (d) the attenuation factor, equivalent (b), (e) storage and (c), (f) loss Young's moduli on beam segment A (with PZT patches) of the 1D A-R shunted smart metamaterials with (a,b,c) the amplifying ratio α or (d), (e), (f) the resistor R when $L = 25$ H. Different colors represent different values of the attenuation factor or the elastic modulus.

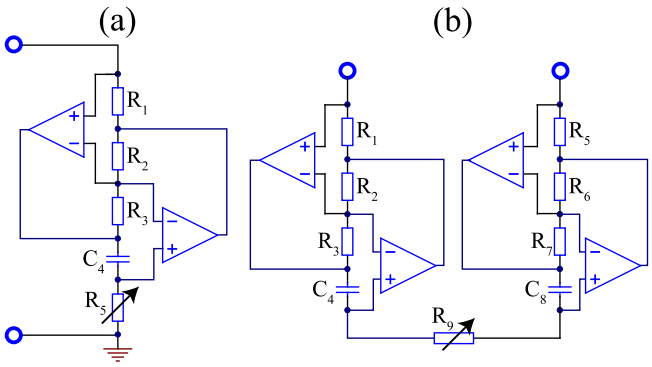

Figure 8. Sketch of two kinds of synthetic inductors: (a) Antoniou's circuit; (b) floating inductor.

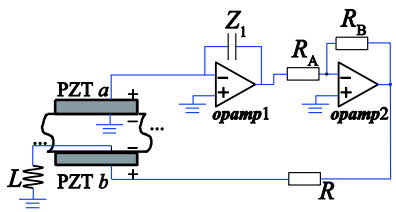

Figure 9. Sketch of one implementation of an A-R shunt circuit with a single reference of ground.

is unnecessary now. In the case of $R_1 = R_5$, $R_2 = R_6$, $R_3 = R_7$ and $C_4 = C_8$, the corresponding inductance is given by

$$L = \frac{R_1 R_3 R_9}{R_2} C_4. \tag{32}$$

In order to enlarge the working voltage range of the circuit, opamp OPA454 from Texas Instruments capable of operating up to ± 50 V is chosen in the implementation of the A-R shunt circuits. One ready-made circuit board is illustrated in figure 10, where two OPA454 chips are used as charge and voltage amplifiers and four OPA454 chips are used to generate a floating inductor. Elements used in the board are listed in table 4.

3.2. Adapting the R-A shunting circuit

As previously mentioned, the in-port resistor R_A of the opamp in the R-A shunting circuit is set to infinity in order to eliminate the parallel connection effect of it and gain better performance. However, for the R-A shunt circuit in its original form [27] as illustrated in figure 11(a), an in-port resistor R_A with large resistance will cause the malfunction of actual opamps. Thus, the in-port resistor R_A of the reverse amplifier needs to be considered as a parallel connection of the RL resonant circuit, which will in turn affects its oscillation.

This limitation can be eliminated by adapting the R-A shunt circuit through inserting a voltage follower depicted in

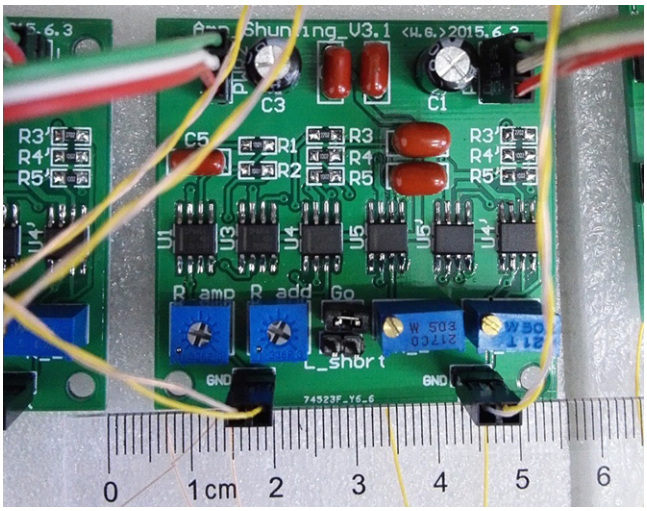

Figure 10. Photo of the A-R shunt circuit board.

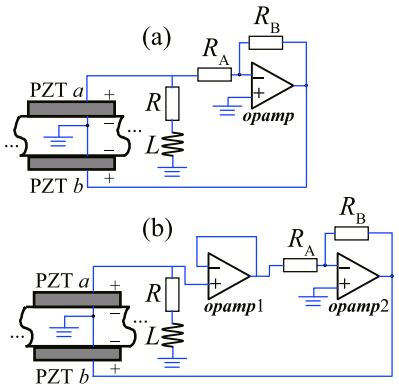

Figure 11. Sketch of the (a) original and (b) adapted A-R shunting circuits.

Table 4. Parameters of elements used in the A-R circuit board.

Parameter	Symbol	Value
Capacitor in charge amplifier	C	15 nF
Resistor A in voltage amplifier	R_A	1 kΩ
Resistor B in voltage amplifier	R_B	20 kΩ (variable)
Resistor 1,5 in inductor	$R_{1,5}$	27 kΩ
Resistor 2,6 in inductor	$R_{2,6}$	10 kΩ
Resistor 3,7 in inductor	$R_{3,7}$	10 kΩ
Capacitor 4,8 in inductor	$C_{4,8}$	330 nF
Resistor 9 in inductor	R_9	(50 + 5) kΩ (variable)
Resistor	R	20 kΩ (variable)

figure 11(b). As the input impedance is very large (e.g. 10^{13} Ω for TI OPA454), it can be omitted in the calculation of impedance connected to PZT patch *a*.

4. FEM simulation

In order to confirm the theoretical results, a finite element model consisting of 765 quadratic Lagrange hexahedral elements is constructed with the commercial FEM software COMSOL, as illustrated in figure 12. In detail, the hosting beam is built with three layers of 3 × 61 elements, while each PZT patch is made of two layers of 3 × 3 elements. The total degrees of freedom (DOF) of the finite element model is 25137. The direct method MUMPS based on LU factorization is used in solving the finite element problem. The effects of shunting circuits is achieved through adapting the elastic constants of PZT patches with equations (8) and (12). A mass of 8 g is added on the right edge of the beam. As for the excitation, a prescribed displacement of 1 in magnitude is added on the left face of the hosting beam. Frequency domain analyses are processed for different circuital parameter sets, where the excitation will be tuned to exp(iωt) automatically. As the excitation is normalized, the resulting displacement on the right face of the beam is the transmission FRF simulated by the FEM. All the results of the FEM simulation are illustrated in figure 16, in comparison with those by theoretical calculations and experimental measurements.

To ensure the accuracy of the FEM simulation, its convergence with different DOFs is examined as shown in figure 13. As a benchmark, the frequencies of the lowest three modal peaks in the vibration transmission FRF (shown as a dash-dotted line in figure 16(a)) of the proposed 1D smart metamaterials (with shorted PZT patches) are chosen in the examination in figure 13. In the figure, FEM simulation results with sparser or denser meshes corresponding to different DOFs (1863, 5175, 10425, 25137 and 61545) are illustrated. The relative error between the results with 25137 and 61545 DOFs is less than 0.4 Hz (0.1%). Actually, the corresponding curves of the vibration transmission FRF nearly coincide. Therefore, the mesh scheme with 25137 DOFs is chosen in the following simulations.

5. Experimental verifications

In order to validate the theoretical results, vibration tests are performed with the experimental devices illustrated in figure 14.

The specimen used in the experiments is the same in theoretical calculations and the FEM simulation. It is made up of an aluminum alloy (6061-T6) beam and six arrays of pairs of PZT (P-42) patches glued on it. The total length of the beam is 0.8 m. Thus a periodic structure with six periods is constructed. Each pair of PZT patches is connected by a uniform ready-made A-R shunting circuit board. The geometric and material parameters are illustrated in tables 1–2, while the circuital parameters used are listed in tables 3–4.

As shown in figure 14, the specimen is hung up by four thin and soft strings in order to generate a free boundary condition. A DC power supply (Zhaoxin RXN-6050D) capable of outputting up to ±60 V is used as the voltage source of the circuit boards.

A block diagram of the experimental system is illustrated in figure 15. White noise signal filtered by a 1 kHz low-pass filter is amplified by the HEAS-20 power amplifier and applied on the HEV-20 exciter. Subsequently, the exciter converts the signal into a vibration excitation and applies it on the left edge

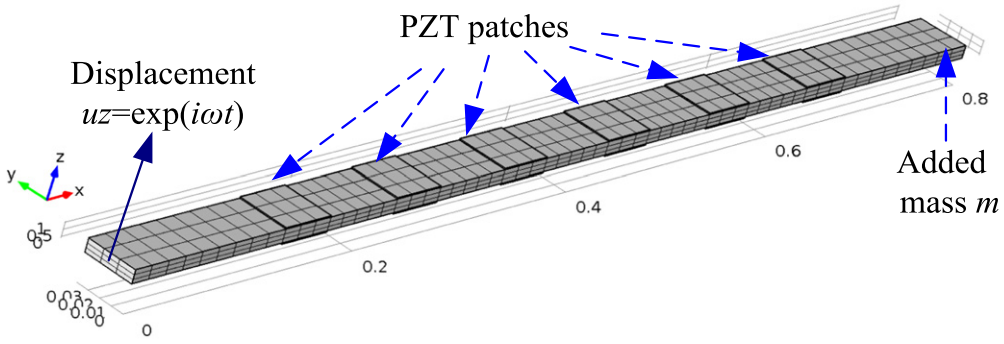

Figure 12. Finite element model of the proposed smart metamaterials.

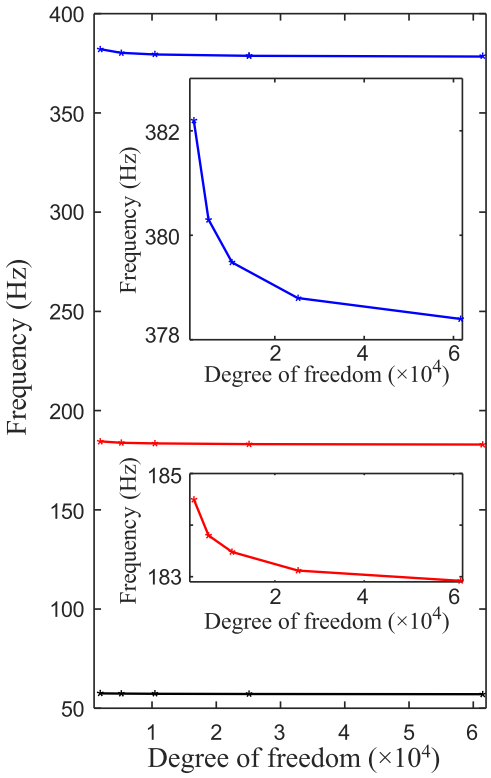

Figure 13. Convergence of the FEM simulation with different DOFs.

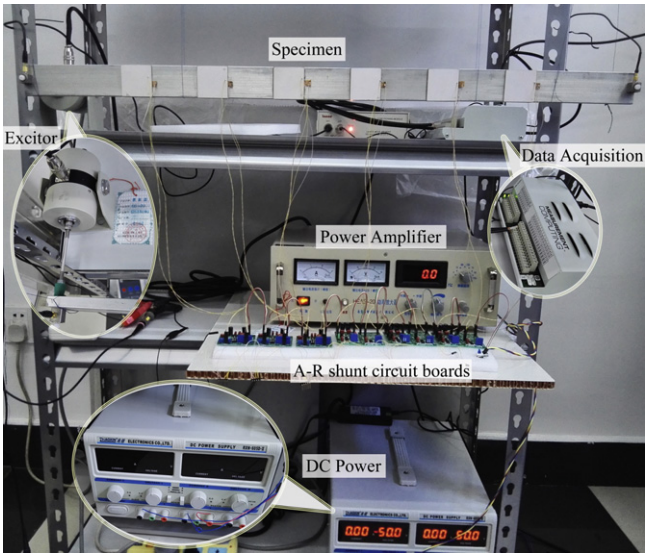

Figure 14. Experimental devices and the specimen.

of the specimen. The vibration responses at both the left and right sides of the specimen are measured in terms of acceleration by two Lance LC0101 accelerometers and then transferred to regular voltage signals by a Lance LC0201-2 signal conditioner. The voltage signals in linear proportion with the accelerations are picked up and tuned to digital data by a USB-1616FS data acquisition board from the Measurement Computing Corporation, and then transferred to the computer via USB cable. Post-processing of all the phase and amplitude data of the vibration responses is conducted in the computer, thus the vibration transmission FRF from points A to B of the specimen is measured with the experimental system.

In figure 16, the measured transmission FRFs (solid lines) of the specimen shunted by the A-R circuits are compared with the corresponding results from TM theoretical calculations (dashed lines) and FEM simulations (dash-dotted lines). Figures 16(b)–(d) illustrate the results when A-R circuits are set to parameter sets 1–3 (see table 3), respectively, while figure 16(a) depicts the case when all the PZT patches are shorted.

From figure 16, one can see that all the measured, calculated and simulated results basically match with respect to frequency ranges/attenuations of band gaps as well as modal frequencies. With different circuital parameter sets of the A-R shunt circuit, the corresponding modal peaks are strongly weakened or even eliminated. The measured drops in the band gap are not as large as the predictions, which is mainly due to the signal–noise limitation of the measurement system where the strongly weakened vibration signal is covered up by noise. Other probable reasons behind mismatches between predicted and experimental results are: wires of accelerometers added on both ends of the beam may cause additional mass and stiffness in the measurement; the unavoidable variance of different shunting circuits; and imprecise material parameters. However, these mismatches are within acceptable ranges.

5.1. Superlattice structure

In order to achieve attenuations in a wider frequency range, a superlattice metamaterial structure is proposed by combining the effects of circuital parameter sets 1–3 together. A sketch

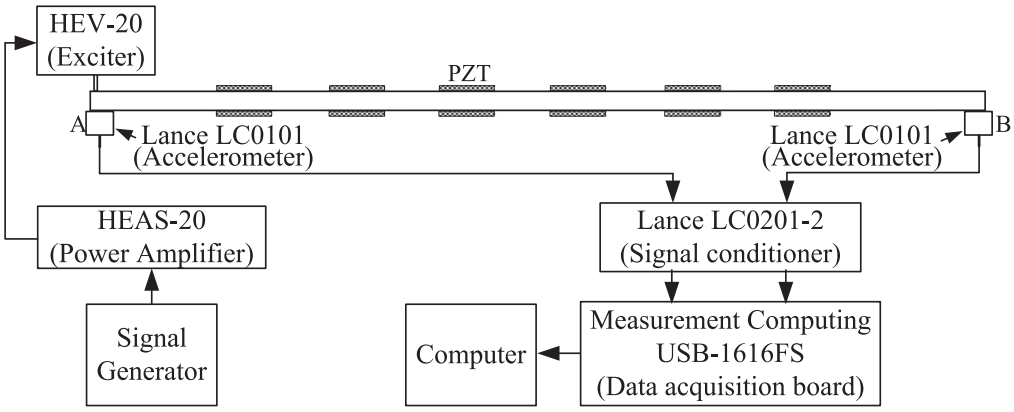

Figure 15. Block diagram of the experimental system.

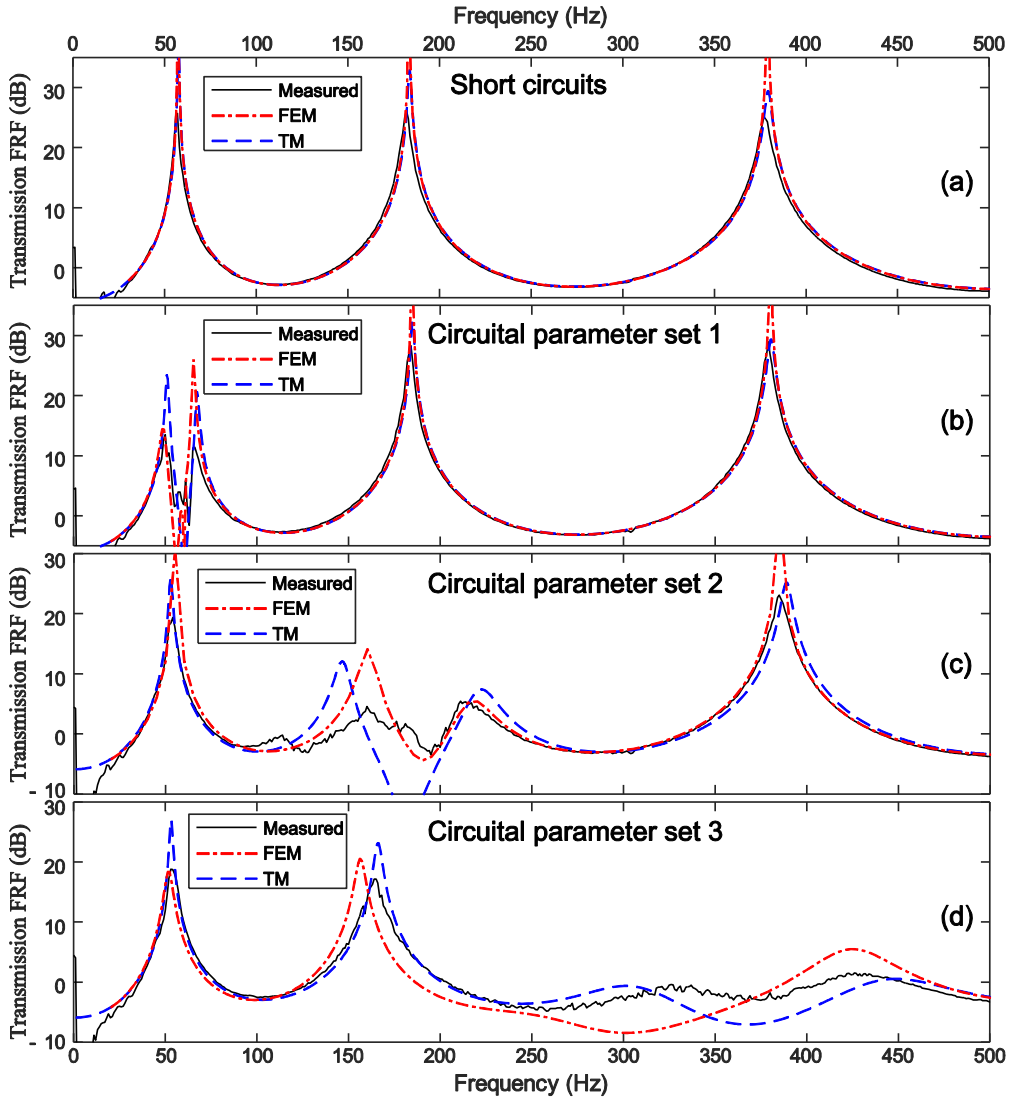

Figure 16. Measured (solid lines), calculated (dashed lines) and simulated (dash-dotted lines) vibration transmission FRFs of the proposed 1D piezoelectric metamaterial beam with A-R shunting circuits. Subfigure (a) represents the results when all PZT patches are shorted, while (b)–(d) correspond to that when A-R shunt circuits are set with parameter sets 1–3, respectively.

of the proposed structure is illustrated in figure 17(a). The dash-dotted box represents the unit cell of the superlattice, which is composed of beam segments A1, A2, A3 and B, where An (n = 1–3) represent the beam segments glued with A-R shunted PZT patches with circuital parameter sets n listed in table 3.

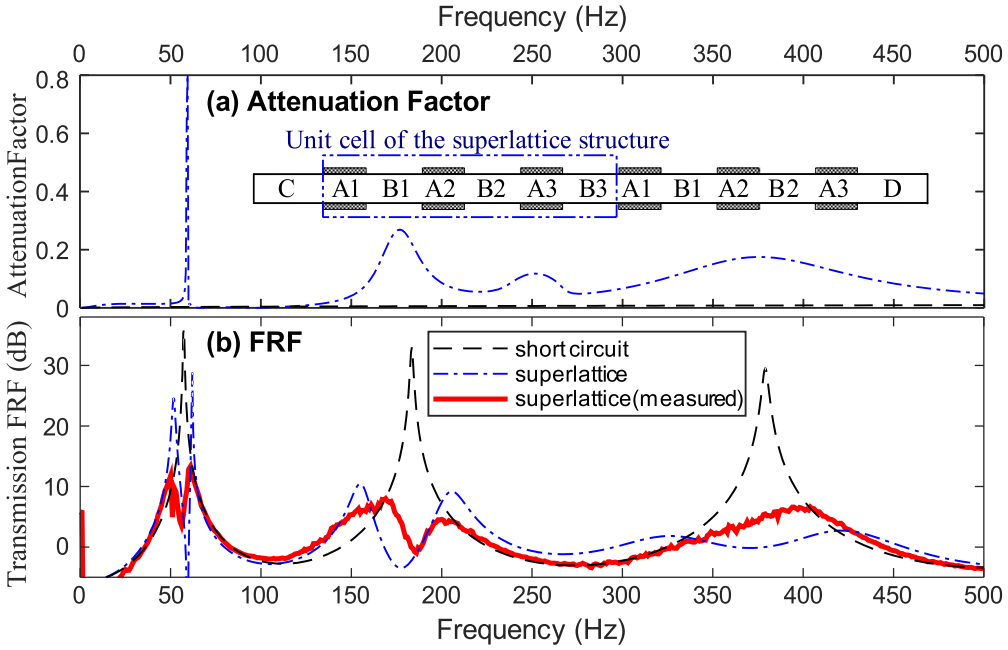

Figure 17. (a) Calculated attenuation factor and sketch of the superlattice metamaterial. (b) Calculated (dash-dotted line) and measured (solid line) vibration transmission FRF of the superlattice metamaterial. The dashed lines in both the two subfigures represent the results when all PZT patches are shorted.

For the superlattice cell, the transfer matrix in equation (20) needs to be rewritten as

$$\begin{aligned}\mathbf{T} = &\left[\mathbf{H}_{\mathrm{A1}}(0)\right]^{-1}\mathbf{H}_{\mathrm{B}}(l_{\mathrm{B}})\left[\mathbf{H}_{\mathrm{B}}(0)\right]^{-1}\mathbf{H}_{\mathrm{A3}}(l_{\mathrm{A}})\\ &\left[\mathbf{H}_{\mathrm{A3}}(0)\right]^{-1}\mathbf{H}_{\mathrm{B}}(l_{\mathrm{B}})\left[\mathbf{H}_{\mathrm{B}}(0)\right]^{-1}\mathbf{H}_{\mathrm{A2}}(l_{\mathrm{A}})\\ &\left[\mathbf{H}_{\mathrm{A2}}(0)\right]^{-1}\mathbf{H}_{\mathrm{B}}(l_{\mathrm{B}})\left[\mathbf{H}_{\mathrm{B}}(0)\right]^{-1}\mathbf{H}_{\mathrm{A1}}(l_{\mathrm{A}})\end{aligned} \tag{33}$$

and the transfer matrix in equation (23) used to calculate the transmission FRF should be

$$\begin{aligned}\mathbf{T}_{\mathrm{all}} = &\left[\mathbf{H}_{\mathrm{D}}(0)\right]^{-1}\mathbf{H}_{\mathrm{A3}}(l_{\mathrm{A}})\left[\mathbf{H}_{\mathrm{A3}}(0)\right]^{-1}\\ &\mathbf{H}_{\mathrm{B}}(l_{\mathrm{B}})\left[\mathbf{H}_{\mathrm{B}}(0)\right]^{-1}\mathbf{H}_{\mathrm{A2}}(l_{\mathrm{A}})\left[\mathbf{H}_{\mathrm{A2}}(0)\right]^{-1}\mathbf{H}_{\mathrm{B}}(l_{\mathrm{B}})\\ &\left[\mathbf{H}_{\mathrm{B}}(0)\right]^{-1}\mathbf{H}_{\mathrm{A1}}(l_{\mathrm{A}})\mathbf{T}^{N-1}\left[\mathbf{H}_{\mathrm{A1}}(0)\right]^{-1}\mathbf{H}_{\mathrm{C}}(l_{\mathrm{C}})\end{aligned} \tag{34}$$

where $\mathbf{H}_{\mathrm{A}n}(l)$ is calculated by equation (19) with circuital parameter sets n listed in table 3.

The calculated attenuation factor and the vibration transmission FRF of the superlattice metamaterial is illustrated as dash-dotted lines in figure 17. A vibration experiment is also conducted on such a structure, and the corresponding measured results are plotted as a solid line in figure 17(b). As before, the dashed lines show the calculated results when all PZT patches are shorted. As the unit cell of the superlattice metamaterial contains three resonant components with different parameters, a combination of their different effects appears in the curves of attenuation factor and transmission FRF. The theoretical and experimental results match well except for some slight differences for similar reasons as discussed before, which is not crucial in the demonstration of this phenomenon. Furthermore, compared with the solid lines in figures 16(b)–(d) which illustrate the measured vibration transmission FRFs of the unilattice metamaterial with circuital sets 1–3, respectively, the result represented as a solid line in figure 17(b) clearly reveals the superlattice combination effect. Although the measured attenuations of superlattice metamaterial specimen cannot reach those of specimens with A-R shunting circuits 1–3 in their particular frequency range, more attenuation frequency ranges can be expected.

6. Conclusions

The vibration attenuation effects of the proposed smart metamaterials composed of an aluminium alloy beam and periodic arrays of PZT patches shunted by A-R circuits are analyzed theoretically and experimentally. It is shown that A-R shunting circuits can evidently increase band gap attenuation compared with passive RSCs and R-A shunting circuits. It is found that the formation of band gap attenuation is due to negative equivalent elastic modulus of the piezoelectric patches at frequencies lower than the resonance. Wider attenuation frequency ranges can be gained by a combination of smart metamaterial cells with different circuital parameters. Finite element simulations as well as vibration experiments were performed to validate the numerical predictions, and demonstrated the effectiveness of the proposed strategy. Compared with other techniques, the proposed strategy provides an efficient way to design smart metamaterials in vibration control.

Acknowledgments

This work was supported by the National Natural Science Foundation of China (Grant No. 51322502).

References

[1] Mead D J 1996 Wave propagation in continuous periodic structures: research contributions from Southampton, 1964-1995 *J. Sound Vib.* **190** 495–524
[2] Yang S, Page J H, Liu Z, Cowan M L, Chan C T and Sheng P 2001 Phononic Crystals *Phy. Canada* **2001** 187–9
[3] Liu Z, Zhang X, Mao Y, Zhu Y Y, Yang Z, Chan C T and Sheng P 2000 Locally resonant sonic materials *Science 289* **289** 1734–6
[4] Hu X, Chan C T and Zi J 2005 Two-dimensional sonic crystals with Helmholtz resonators *Phys. Rev.* E **71** 055601
[5] Wang G, Wen X, Wen J, Shao L and Liu Y 2004 Two-dimensional locally resonant phononic crystals with binary structures *Phys. Rev. Lett.* **93** 154302
[6] Fang N, Xi D, Xu J, Ambati M, Srituravanich W, Sun C and Zhang X 2006 Ultrasonic metamaterials with negative modulus *Nat. Mater.* **5** 452–6
[7] Wen J, Yu D, Wang G and Wen X 2008 Directional propagation characteristics of flexural wave in two-dimensional periodic grid-like structures *J. Phys. D Appl. Phys.* **41** 135505
[8] Hagood N W and Von Flotow A 1991 Damping of structural vibrations with piezoelectric materials and passive electrical network *J. Sound Vib.* **146** 243–68
[9] Ruzzene M and Baz A 2001 Active control of wave propagation in periodic fluid-loaded shells *Smart Mater. Struct.* **10** 893–906
[10] Thorp O, Ruzzene M and Baz A 2001 Attenuation and localization of wave propagation in rods with periodic shunted piezoelectric patches *Smart Mater. Struct.* **10** 979–89
[11] Airoldi L and Ruzzene M 2011 Wave propagation control in beams through periodic multi-branch shunts *J. Intell. Mater. Syst. Struct.* **22** 1567–79
[12] Airoldi L and Ruzzene M 2011 Design of tunable acoustic metamaterials through periodic arrays of resonant shunted piezos *New J. Phys.* **13** 113010
[13] Chen S, Wen J, Wang G, Yu D and Wen X 2012 Improved modeling of rods with periodic arrays of shunted piezoelectric patches *J. Intell. Mater. Syst. Struct.* **23** 1613–21
[14] Wang G, Chen S and Wen J 2011 Low-frequency locally resonant band gaps induced by arrays of resonant shunts with Antoniou's circuit: experimental investigation on beams *Smart Mater. Struct.* **20** 015026
[15] Casadei F, Beck B S, Cunefare K A and Ruzzene M 2012 Vibration control of plates through hybrid configurations of periodic piezoelectric shunts *J. Intell. Mater. Syst. Struct.* **23** 1169–77
[16] Casadei F, Ruzzene M, Dozio L and Cunefare K A 2010 Broadband vibration control through periodic arrays of resonant shunts: experimental investigation on plates *Smart Mater. Struct.* **19** 015002
[17] Spadoni A, Ruzzene M and Cunefare K 2009 Vibration and wave propagation control of plates with periodic arrays of shunted piezoelectric patches *J. Intell. Mater. Syst. Struct.* **20** 979–90
[18] Wen J, Chen S, Wang G, Yu D and Wen X 2014 Directionality of wave propagation and attenuation in plates with resonant shunting arrays *J. Intell. Mater. Syst. Struct.* in press
[19] Chen S, Wang G, Wen J and Wen X 2013 Wave propagation and attenuation in plates with periodic arrays of shunted piezo-patches *J. Sound Vib.* **332** 1520–32
[20] Forward R L 1979 Electronic damping of vibrations in optical structures *J. Appl. Opt.* **18** 690–7
[21] Behrens S, Fleming A J and Moheimani S O R 2003 A broadband controller for shunt piezoelectric damping of structural vibration *Smart Mater. Struct.* **12** 18–28
[22] Park C H and Baz A 2005 Vibration control of beams with negative capacitive shunting of interdigital electrode piezoceramics *J. Sound Vib.* **11** 331–46
[23] Neubauer M, Oleskiewicz R, Popp K and Krzyzynski T 2006 Optimization of damping and absorbing performance of shunted piezo elements utilizing negative capacitance *J. Sound Vib.* **298** 84–107
[24] Beck B S, Cunefare K A, Ruzzene M and Collet M 2011 Experimental analysis of a cantilever beam with a shunted piezoelectric periodic array *J. Intell. Mater. Syst. Struct.* **22** 1177–87
[25] Tateo F, Collet M, Ouisse M, Ichchou M, Cunefare K and Abbe P 2014 Experimental characterization of a bi-dimensional array of negative capacitance piezo-patches for vibroacoustic control *J. Intell. Mater. Syst. Struct.* **26** 952–64
[26] de Marneffe B and Preumont A 2008 Vibration damping with negative capacitance shunts: theory and experiment *Smart Mater. Struct.* **17** 035015
[27] Wang G, Wang J, Chen S and Wen J 2011 Vibration attenuations induced by periodic arrays of piezoelectric patches connected by enhanced resonant shunting circuits *Smart Mater. Struct.* **20** 125019
[28] Yamada K, Matsuhisa H and Utsuno H 2014 Enhancement of efficiency of vibration suppression using piezoelectric elements and LR circuit by amplification of electrical resonance *J. Sound Vib.* **333** 1281–301
[29] Antoniou A 1969 Realization of gyrators using operational amplifiers, and their use in RC-active-network synthesis *Proc. IEEE* **116** 1838–50
[30] Ashcroft N W and Mermin N D 1976 *Solid State Physics* (Philadelphia, PA: Saunders College)
[31] Moheimani S O R and Fleming A J 2006 *Piezoelectric Transducers for Vibration Control and Damping* (London: Springer)